A flux-controlled model of meminductor and its application in chaotic oscillator*

Guang-Yi Wang(王光义)[1], Pei-Pei Jin(靳培培)[1], Xiao-Wei Wang(王晓炜)[2,†], Yi-Ran Shen(沈怡然)[1], Fang Yuan(袁方)[1], and Xiao-Yuan Wang(王晓媛)[1]

[1] *Key Laboratory of RF Circuits and Systems (Ministry of Education), Institute of Modern Circuits and Intelligent Information, Hangzhou Dianzi University, Hangzhou* 310018, *China*

[2] *Department of Automation, Shanghai University, Shanghai* 200072, *China*

(Received 24 February 2016; revised manuscript received 26 April 2016; published online 19 July 2016)

A meminductor is a new type of memory device developed from the memristor. We present a mathematical model of a flux-controlled meminductor and its equivalent circuit model for exploring the properties of the meminductor in a nonlinear circuit. We explore the response characteristics of the meminductor under the exciting signals of sinusoidal, square, and triangular waves by using theoretical analysis and experimental tests, and design a meminductor-based oscillator based on the model. Theoretical analysis and experiments show that the meminductor-based oscillator possesses complex bifurcation behaviors and can generate periodic and chaotic oscillations. A special phenomenon called the co-existent oscillation that can generate multiple oscillations (such as chaotic, periodic oscillations as well as stable equilibrium) with the same parameters and different initial conditions occurs. We also design an analog circuit to realize the meminductor-based oscillator, and the circuit experiment results are in accordance with the theory analysis.

Keywords: meminductor, oscillator, chaos, co-existent attractor

PACS: 05.45.–a, 05.45.Jn, 05.45.Pq **DOI:** 10.1088/1674-1056/25/9/090502

1. Introduction

As a novel memory device, the memristor was proposed by Chua as early as 1971.[1] Since Strukov *et al.* realized a physical memristor by nanotechnology,[2] the research of the memristor and its application circuits has gained rapid progress world wide. The meminductor and memcapacitor are members of a large family of new circuit elements postulated by Chua in his guest lecture at the 1978 European Conference on Circuit Theory and Design (ECCTD).[3] The meminductor and memcapacitor were formally defined by Chua in 2003.[4] In particular, the memristor can be identified as a higher-order element $(-1, -1)$, the meminductor can be identified as a higher-order element $(-2, -1)$, and the memcapacitor can be identified as a higher-order element $(-1, -2)$. More recently, the meminductor and memcapacitor were presented, along with their standard symbols, at the keynote lecture of the First Symposium on Memristors, held in Berkeley, California in 2008.[5] A tutorial on the memcapacitor and meminductor was presented in the last section of the IEEE Expert Now SHORT Course.[6] Readers are encouraged to read the tutorial in order to have a deeper understanding of the present paper.

The memristor, memcapacitor, and meminductor are all passive memory devices which can store information without a power supply. Because of their unique memory and dynamical storage ability, they can be used in the fields such as non-volatile storage and simulations of learning, adaptive, and spontaneous behaviors.[7,8] In the meantime, the applications of these memory devices in nonlinear circuits has gained a great deal of attention.

As the representative of memory devices, the memristor appeared earliest in nonlinear circuits. At present, the models of the memristor mostly adopt a piecewise linear, quadratic, or cubic smooth function[9–11] as the charge–flux relationship. All the above models are ideal, and the HP TiO_2 physical model is more practical to the needs of applications. Compared with the memristor, the memcapacitor and meminductor have been much less studied because they have not yet been realized physically and their mathematical models are not as perfect as that of the memristor.[12] So we do not know much about their properties in nonlinear circuits.

Although the physical meminductor has not appeared, its potential value has attracted many researchers. In 2011, the Pershin group[13] reported the accomplishment of modeling the memristor, meminductor, and memcapacitor. Then the simulation of the meminductor was realized by using controlled sources and programed modules.[14] Further, a circuit-easily realized equivalent circuit model was proposed by using the transfer relationship between the memristor and meminductor.[15] In Ref. [16], a mathematical model of the

*Project supported by the National Natural Science Foundation of China (Grant Nos. 61271064, 61401134, and 60971046), the Natural Science Foundation of Zhejiang Province, China (Grant Nos. LZ12F01001 and LQ14F010008), and the Program for Zhejiang Leading Team of S&T Innovation, China (Grant No. 2010R50010).

†Corresponding author. E-mail: laura423_wang@163.com

© 2016 Chinese Physical Society and IOP Publishing Ltd

meminductor was proposed by using the fraction calculus. In Ref. [17], an approximate equivalent circuit of a meminductor imitated by a memristor was presented. In Ref. [18], an easily realized cubic-smooth active flux-controlled memristor instead of the digital memristor circuit in Ref. [17] was designed. An analysis of the meminductor properties was carried out and an approximate meminductor equivalent circuit simulation and experimental verification were done by using the equivalent circuit of a memristor. Furthermore, in Ref. [19], an efficient method was proposed to build a mutator-based meminductor (ML) model whose inductance can be varied by an external current source.

From the above, we can see that these meminductor models are all ideal. In fact, the memristive behaviors are more readily observable and significant at the nanoscale,[5,20,21] and the properties of the memristor, meminductor, and memcapacitor are common at the nanoscale.[5] Hence, in this paper, we propose an HP memristor-like meminductor model, which conforms more to the future achievable physical one. Based on the proposed flux-controlled model of a meminductor, an equivalent circuit for imitating the behaviors of the meminductor model is designed and realized. The responses for the excitations of waves of sine, pulse, and triangle are verified respectively via the equivalent circuit experiments of the meminductor model. Based on the model, a chaotic oscillator circuit is designed and physically realized. The dynamical behaviors of the oscillator circuit such as periodic oscillation, chaotic oscillation, and their bifurcations are analyzed by theoretical analysis, simulation and circuit experiments, and the results of the experiments are in accordance with the theory analysis and simulations.

2. Models of flux-controlled meminductor

2.1. Mathematical model

It has been found that some microsystems exhibit meminductive properties.[5,20,21] Hence, we can deduce a mathematical model of a meminductor from the nanoscale HP memristor model, and it can be called the HP memristor-like model.

According to Ref. [2], the HP TiO_2 memristor has the following model:

$$\begin{cases} u(t) = \left[R_{\rm on}\dfrac{w(t)}{D} + R_{\rm off}\left(1-\dfrac{w(t)}{D}\right)\right] i(t), \\ \dfrac{{\rm d}w(t)}{{\rm d}t} = \dfrac{\mu_v R_{\rm on}}{D} i(t), \quad w(t) = \dfrac{\mu_v R_{\rm on}}{D} q(t), \end{cases} \tag{1}$$

where $u(t)$, $i(t)$, and $q(t)$ denote the voltage, current, and charge across the memristor; $R_{\rm on}$ and $R_{\rm off}$ stand for the resistances of the high doping domain and the low doping domain, respectively; D and w represent the thicknesses of the whole domain between two boards of platinum electodes and the doping TiO_2 layer, respectively; and μ_v denotes the dopant mobility. According to Eq. (1), the resistance of the memristor can be calculated as

$$M_R = R_{\rm off} + \frac{(R_{\rm on}-R_{\rm off})\mu_v R_{\rm on}}{D^2} q(t). \tag{2}$$

Let $\alpha = R_{\rm off}$ and $\beta = (R_{\rm on}-R_{\rm off})u_v R_{\rm on}/D^2$, we obtain the simplified model as

$$M_R = \alpha + \beta q(t) = \alpha + \beta \int_{t_0}^{t} i(\tau)\,{\rm d}\tau, \tag{3}$$

$$u(t) = [\alpha + \beta q(t)]i(t) = [\alpha + \beta \int_{t_0}^{t} i(\tau)\,{\rm d}\tau]i(t). \tag{4}$$

Memristance and memductance follow the same law except they are reciprocal. So we can write down the mathematical expression of memductance according to Eq. (4)

$$i(t) = [a + b\varphi(t)]u(t) = \left[a + b\int_{t_0}^{t} u(\tau)\,{\rm d}\tau\right]u(t), \tag{5}$$

where $\varphi(t)$ is the flux across the memristor.

A meminductor, by contrast to a memresistor, has the definition that it is a two-port passive device whose properties depend on the state and its history. The current through the meminductor relate to its flux, typically showing a pinched hysteretic loop between the flux and the current.

Ventra *et al.* defined the current-controlled and the flux-controlled meminductors,[5] which are described as follows:

$$\begin{aligned} &\varphi(t) = L_{\rm M}(x,i,t)i(t), \dot{x} = f(x,i,t); \\ &i(t) = L_{\rm M}^{-1}(x,\varphi,t)\varphi(t), \dot{x} = f(x,\varphi,t); \end{aligned} \tag{6}$$

where x is an internal state variable, $\varphi(t)$ and $i(t)$ are the flux and the current across the meminductor, and $L_{\rm M}$ and $L_{\rm M}^{-1}$ are the meminductance and the inverse meminductance, respectively. From the above, we can conclude that both $L_{\rm M}$ and $L_{\rm M}^{-1}$ are time-varying functions of current and flux. Analogous to Eqs. (1)–(5), we obtain the simplified model of the meminductor as

$$\varphi(t) = [\alpha + \beta q(t)]i(t) = [\alpha + \beta \int_{t_0}^{t} i(\tau)\,{\rm d}\tau]i(t), \tag{7}$$

$$i(t) = [\alpha + \beta \rho(t)]\varphi(t) = [\alpha + \beta \int_{t_0}^{t} \varphi(\tau)\,{\rm d}\tau]\varphi(t). \tag{8}$$

We usually adopt the form of inverse meminductance in practice

$$L_{\rm M}^{-1}(\rho) = \alpha + \beta\rho(t), \tag{9}$$

where $\rho(t) = \int_{t_0}^{t} \varphi(\tau)\,{\rm d}\tau$ is the integral variable of the flux. By integrating two sides of Eq. (8), we obtain the mathematical model of the meminductor

$$q(t) = \alpha\rho(t) + \frac{1}{2}\beta\rho(t)^2, \tag{10}$$

which defines the relationship between the charge $q(t)$ and the integral variable $\rho(t)$.

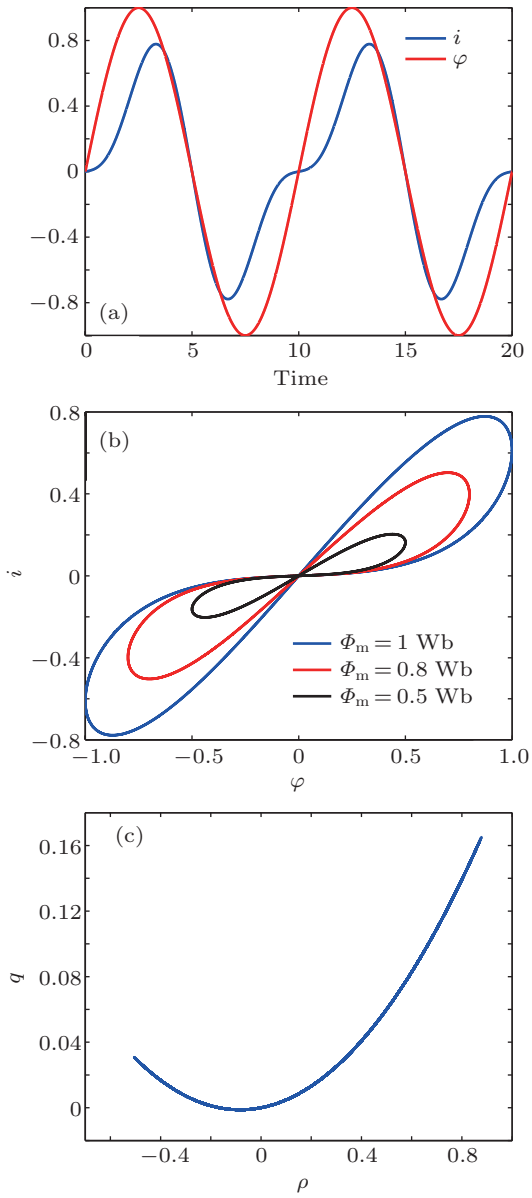


Fig. 1. (color online) (a) Waveforms of current and flux for the flux-controlled meminductor; (b) pinched hysteresis loop of flux-current; (c) ρ–q characteristic.

Let $\alpha = 0.03$, $\beta = 0.36$, and $\varphi(t) = \Phi_{\rm m}\sin(2\pi Ft)$, according to Eq. (8), the current through the meminductor can be described as

$$\begin{aligned} i(t) &= [\alpha + \beta \int_{t_0}^{t} \Phi_{\rm m}\sin\omega\tau \,{\rm d}\tau]\Phi_{\rm m}\sin\omega t \\ &= a\sin\omega t - b\sin 2\omega t, \end{aligned}$$

where $a = \alpha\Phi_{\rm m} + \beta\Phi_{\rm m}^2\cos\omega t_0/\omega$ and $b = \beta\Phi_{\rm m}^2/2\omega$.

The time domain waveforms of the current and the flux are shown in Fig. 1. Let $\Phi_{\rm m} = 1$ Wb, $\Phi_{\rm m} = 0.8$ Wb, and $\Phi_{\rm m} = 0.5$ Wb, based on Eq. (8), we obtain the typical pinched hysteretic loops in the two constitutive variables, flux vs. current, as shown in Fig. 1(b); and let $\Phi_{\rm m} = 1$ Wb, the phase portrait of ρ and q is pictured in Fig. 1(c) based on Eq. (10).

2.2. Equivalent circuit model

An equivalent circuit is important for the meminductor research since a physical meminductor has not been realized. The equivalent circuit model based on Eq. (8) is shown in Fig. 2, which is composed of five operational amplifiers and one multiplier. The operational amplifiers are all LF347 and the multiplier is AD633. Voltage u is the input of the equivalent circuit. Nodes i and φ are the test points of the current and the flux, respectively. From the output of the inverse integrator constructed by U_1, C_1, R_1, and R_2, we can obtain the flux signal $-\varphi(t) = -\int_{t_0}^{t} u(\tau)\,{\rm d}\tau$. Then the flux $-\varphi(t)$ passes through the inverter consisting of U_2, R_3, and R_5, and $\varphi(t)$ is obtained from its output as the input of the adder consisting of U_4 and R_7–R_9. In the mean time, the output, $-\varphi(t)$, of U_1 passes through the inverse integrator constructed by U_3, C_2, R_4, and R_6, and then the integral signal $\rho(t) = \int_{t_0}^{t}\varphi(\tau)\,{\rm d}\tau$ is obtained from the output. The signal $\rho(t)$ passes through the multiplier and the product term $\rho(t)\varphi(t)$ is obtained. Then the product term is sent to the input of the adder. Finally, at the output of U_4, we obtain the current

$$i(t) = \left[\frac{R_{11}}{R_{10}}\frac{R_9}{R_7} + \frac{R_{11}}{R_{10}}\frac{R_9}{R_8}\rho(t)\right]\varphi(t),$$

which realize the relationship between current $i(t)$ and flux $\varphi(t)$ for the meminductor. Comparing with Eq. (10), we have $\alpha = R_{11}R_9/R_{10}R_7$ and $\beta = R_{11}R_9/R_{10}R_8$.

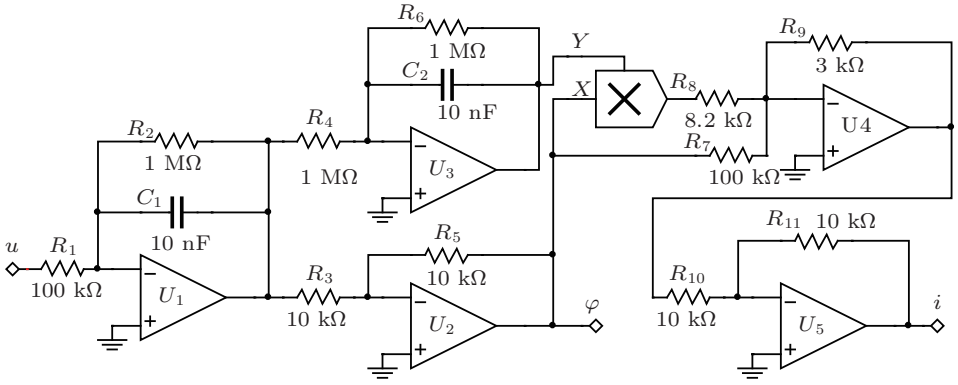


Fig. 2. Equivalent circuit of the flux-controlled memindutor with φ–i property.

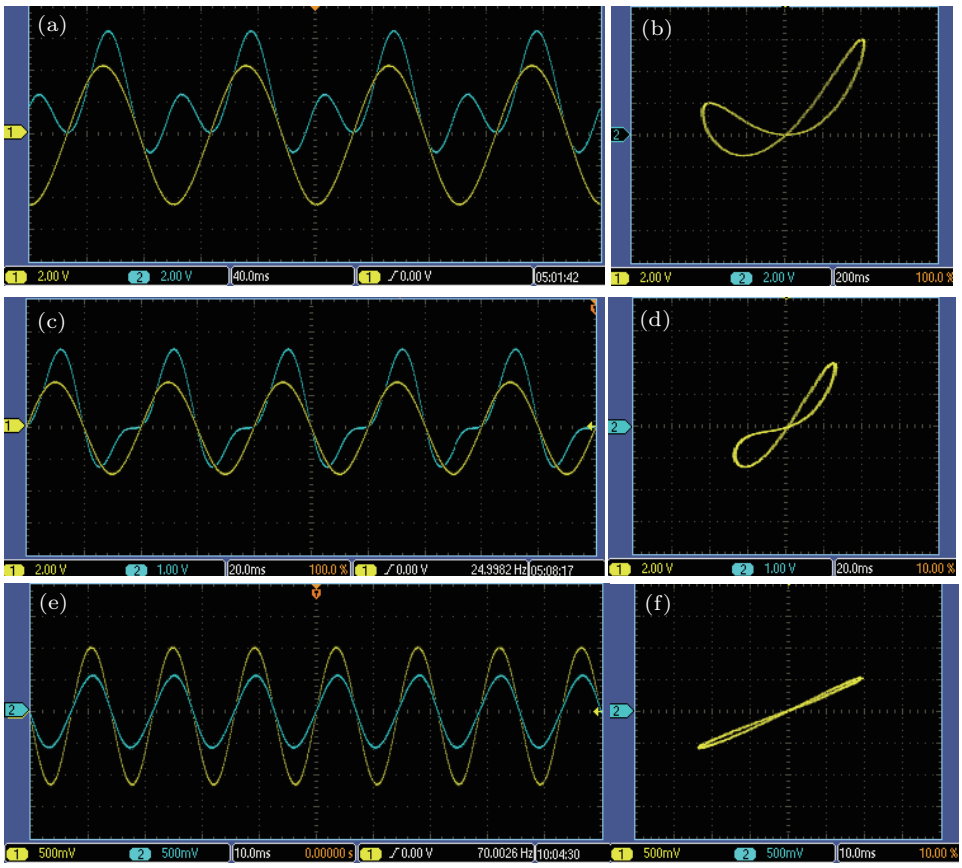


Fig. 3. (color online) Experimental current (green) and flux (yellow) waveforms and the corresponding pinched hysteresis loops for the equivalent meminductor circuit with a sinusoidal input at the frequency of: (a), (b) 10 Hz; (c), (d) 25 Hz; (e), (f) 70 Hz.

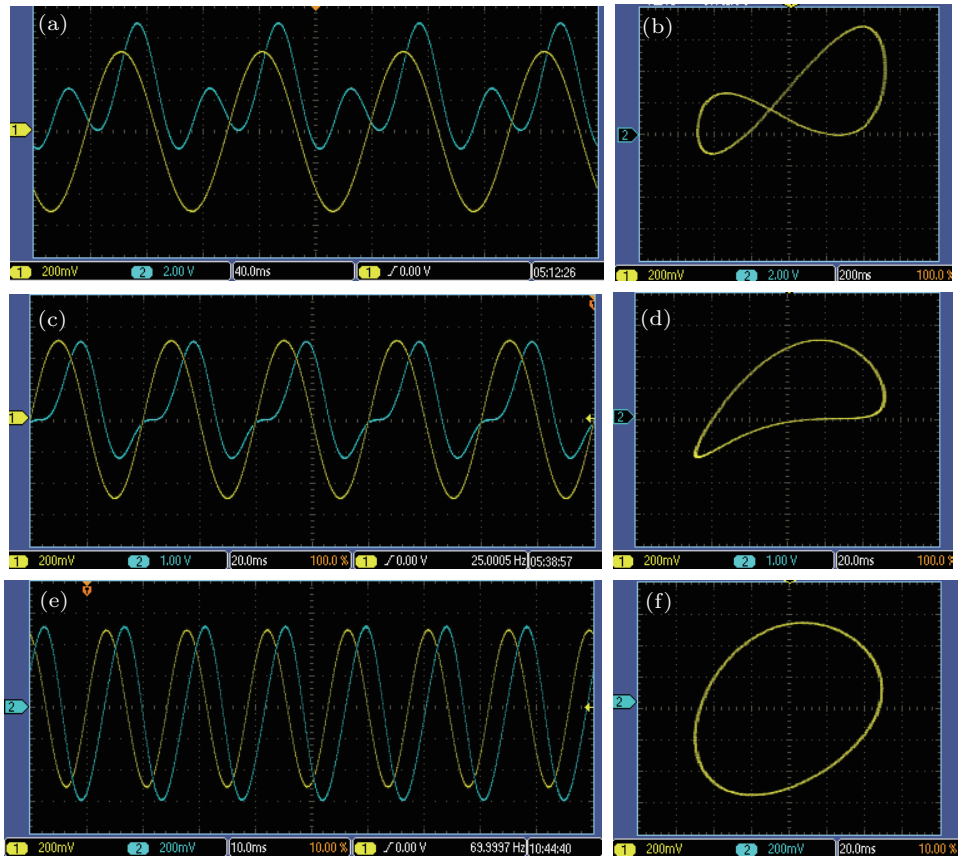


Fig. 4. (color online) Experimental current (green) and voltage (yellow) waveforms and the corresponding phase diagrams for the equivalent meminductor circuit with a sinusoidal input at the frequency of: (a), (b) 10 Hz; (c), (d) 25 Hz; (e), (f) 70 Hz.

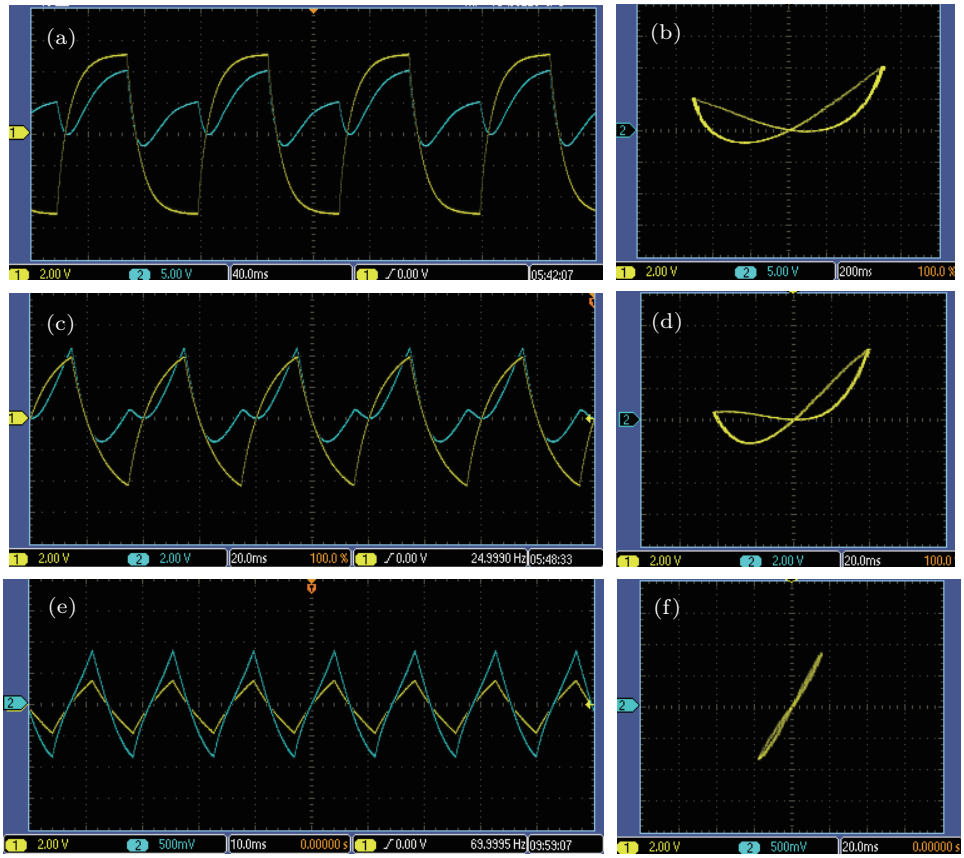


Fig. 5. (color online) Experimental current (green) and flux (yellow) waveforms and the corresponding pinched hysteresis loops for the equivalent meminductor circuit with a square-wavel input at the frequency of: (a), (b) 10 Hz; (c), (d) 25 Hz; (e), (f) 70 Hz.

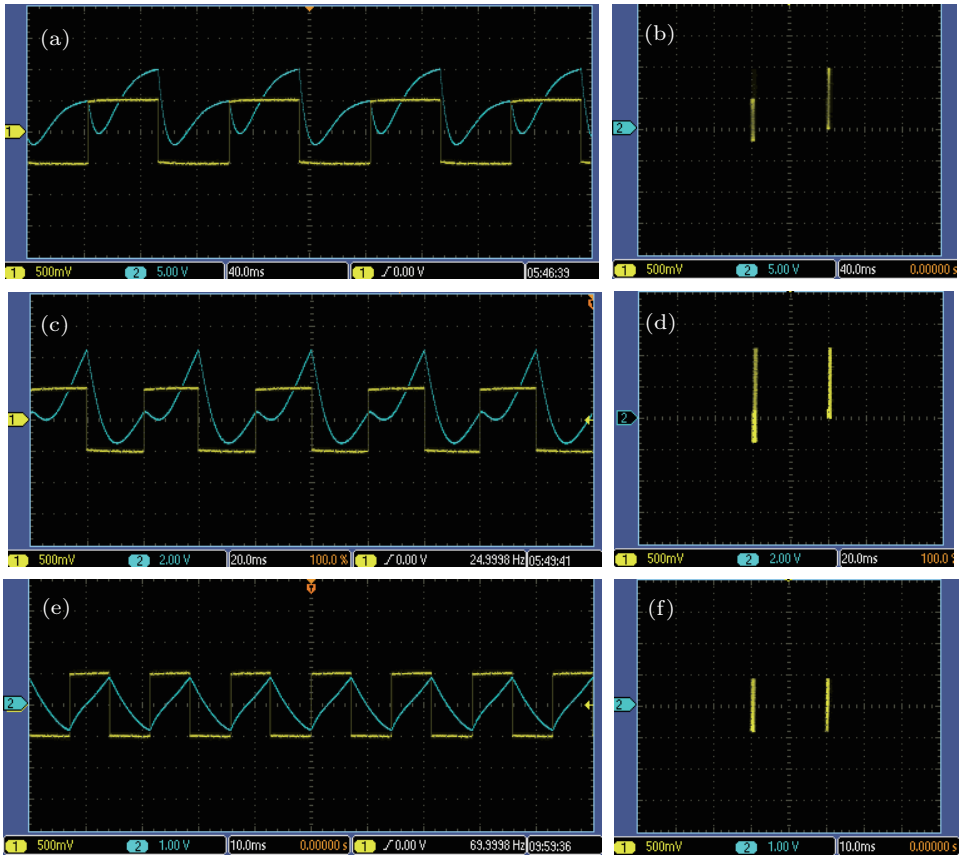


Fig. 6. (color online) Experimental current (green) and voltage (yellow) waveforms and the corresponding phase diagrams for the equivalent meminductor circuit with a square-wavel input at the frequency of: (a), (b) 10 Hz; (c), (d) 25 Hz; (e), (f) 70 Hz.

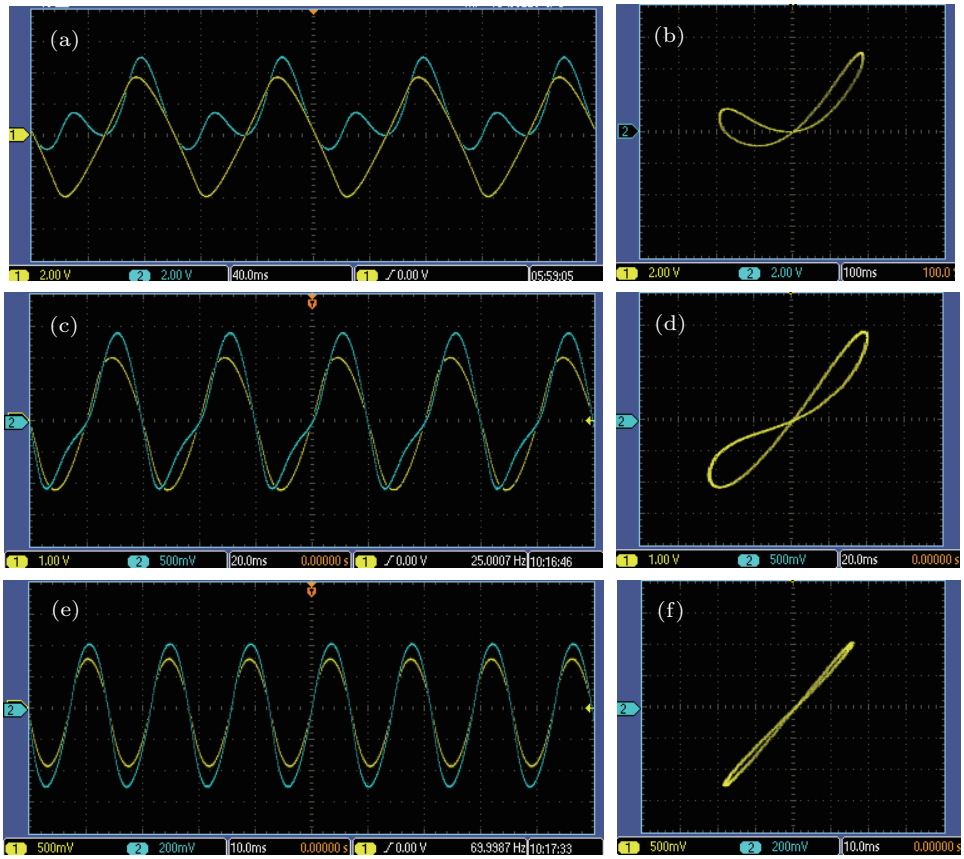


Fig. 7. (color online) Experimental current (green) and flux (yellow) waveforms and the corresponding pinched hysteresis loops for the equivalent meminductor circuit with a triangle input voltage at the frequency of: (a), (b) 10 Hz; (c), (d) 25 Hz; (e), (f) 70 Hz.

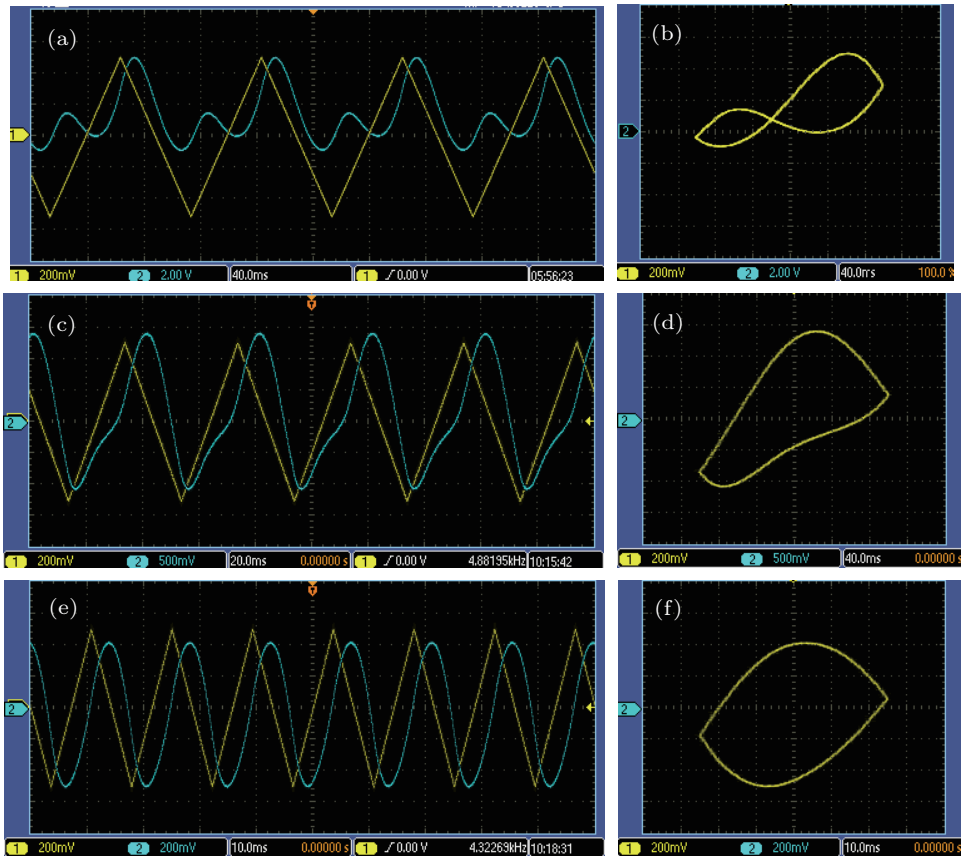


Fig. 8. (color online) Experimental current (green) and voltage (yellow) waveforms and the corresponding phase diagrams for the equivalent meminductor circuit with a triangle input voltage at the frequency of: (a), (b) 10 Hz; (c), (d) 25 Hz; (e), (f) 70 Hz.

We have built an equivalent circuit to emulate the features of the meminductor. Now the feasibility of the circuit is proved with hardwire experiments. Figure 3 shows the oscilloscope displays of i (green)–φ (yellow) waveforms and the corresponding pinched hysteresis loops from the hardwire experiments, in which the input signal is sine voltage $U_{\rm m}\sin 2\pi ft$ with different frequencies. Figure 4 shows the experimental waveforms of current i (green) and voltage u (yellow) as well as the corresponding pinched hysteresis loops from the hardwire experiments with the sine input $U_{\rm m}\sin 2\pi ft$.

From Figs. 3 and 4, we can see that the pinched hysteresis loops defining the meminductor must pass through the origin of the flux vs. current plane under all bipolar periodic excitations in either flux or current, and gradually become a straight line with the increase of the sine frequency, as shown in Figs. 3(b), 3(d), and 3(f). However, the phase portrait of the current vs. voltage for the same meminductor may not pass through the origin, and can be a circle instead of a pinched hysteresis loop, as shown in Figs. 4(b), 4(d), and 4(f). The frequency dependence of the pinched hysteresis loop is a unique feature of the meminductor.

When we use a square-wave voltage to drive the equivalent meminductor circuit, the experimental waveforms of current i (green) and flux φ (yellow) and the corresponding pinched hysteresis loops from the hardwire experiment at different square-wave frequencies are shown in Fig. 5, and the corresponding experimental waveforms and phase portraits for current i and voltage u are shown in Fig. 6.

Figures 7 and 8 show the experimental results with a triangle input voltage at different frequency for the current i (green)–flux φ (yellow) and the current i (green)–voltage u (yellow), respectively.

Note again that although the pinched hysteresis loops must pass through the origin of the flux vs. current plane under bipolar periodic excitation in either flux or current, the phase portrait of the current vs. voltage can be a circle not passing through the origin, as shown in Figs. 5–8.

2.3. Equivalent circuit model of the ρ–q property for the meminductor

The equivalent circuit model of the ρ–q property for the meminductor based on Eq. (10) is shown in Fig. 9, which includes three operational amplifiers and one multiplier.

The input signal ρ, which equals the time integral of the flux, becomes ρ^2 after passing the multiplier A_2, and then it becomes $-\rho^2$ at the output of U_6. In another terminal, ρ passes through the inverter consisting of U_5, R_{10}, and R_{11}, and then we obtain $-\rho$ from its output. Finally, at the output of the adder composed of U_7, R_{15}, and R_{16}, we obtain

$$q = \frac{R_{16}}{R_{13}}\rho + \frac{R_{16}}{R_{15}}\rho^2,$$

which realizes the ρ–q relationship described by Eq. (10). The phase diagram of flux ρ vs. charge q is described in Fig. 10, which is obtained from the simulation using Multisim.

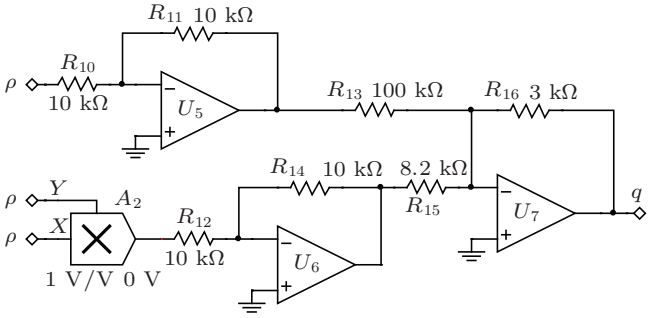


Fig. 9. Equivalent circuit of the flux-controlled meminductor with the ρ–q property.

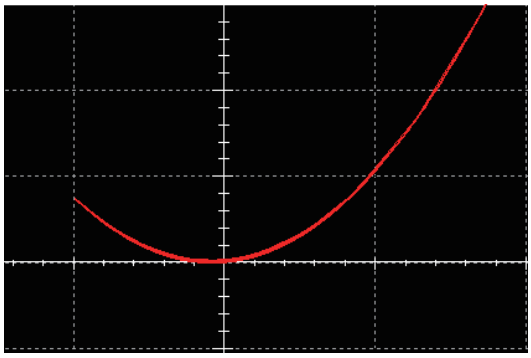


Fig. 10. (color online) Phase diagram of ρ–q.

3. Meminductor-based oscillator

3.1. Oscillator circuit

Reference [22] reported the simplest chaotic circuit, which uses only a linear passive inductor, a linear passive capacitor, and a nonlinear active memristor, and shows several attractors. Here, we present an oscillator circuit in Fig. 11 based on the proposed meminductor model in this paper. The oscillator circuit is composed of a resistor, a negative resistor labeled with the negative conductance $-G$, two capacitors, and a nonlinear element, namely, the flux-controlled meminductor. The negative resistor is used to supply the circuit with energy for maintaining the oscillation.

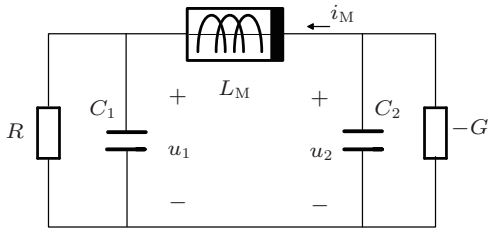


Fig. 11. Meminductor-based oscillator circuit.

We take capacitor voltages u_1, u_2 and flux φ of the meminductor as the state variables. By applying Kirchhoff's laws

to this circuit, the governing equations are obtained as

$$\begin{cases} \dfrac{\mathrm{d}u_1}{\mathrm{d}t} = \dfrac{1}{C_1}\left(i_{\mathrm{M}} - \dfrac{u_1}{R}\right), \\ \dfrac{\mathrm{d}u_2}{\mathrm{d}t} = \dfrac{1}{C_2}(Gu_2 - i_{\mathrm{M}}), \\ \dfrac{\mathrm{d}\varphi}{\mathrm{d}t} = u_2 - u_1. \end{cases} \tag{11}$$

By inserting the model $i_{\mathrm{M}} = [\alpha + \beta\rho(t)]\varphi(t)$ and adding the equation $\mathrm{d}\rho/\mathrm{d}t = \varphi$ into Eq. (11) respectively, and setting $a = \alpha/C_1$, $b = \beta/C_1$, $c = 1/(C_1R)$, $d = G/C_2$, $e = \alpha/C_2$, and $f = \beta/C_2$, equation (11) can be given as

$$\begin{cases} \dfrac{\mathrm{d}u_1}{\mathrm{d}t} = a\varphi + b\varphi\rho - cu_1, \\ \dfrac{\mathrm{d}u_2}{\mathrm{d}t} = \mathrm{d}u_2 - e\varphi - f\varphi\rho, \\ \dfrac{\mathrm{d}\varphi}{\mathrm{d}t} = u_2 - u_1, \\ \dfrac{\mathrm{d}\rho}{\mathrm{d}t} = \varphi. \end{cases} \tag{12}$$

With suitable parameters, this circuit can exhibit periodic and chaotic oscillations. For example, with $a = 1.0$, $b = 6.0$, $c = 4.6$, $d = 0.4$, $e = 4.0$, and $f = 1.0$, the oscillator generates a periodic signal; while if $d = 0.7$ (the other parameters stay the same), the oscillator is in a chaotic state. The generated periodic and chaotic waveforms of voltage u_2 are shown in Fig. 12, and the chaotic phase portraits, namely, the chaotic attractors, are described in Fig. 13.

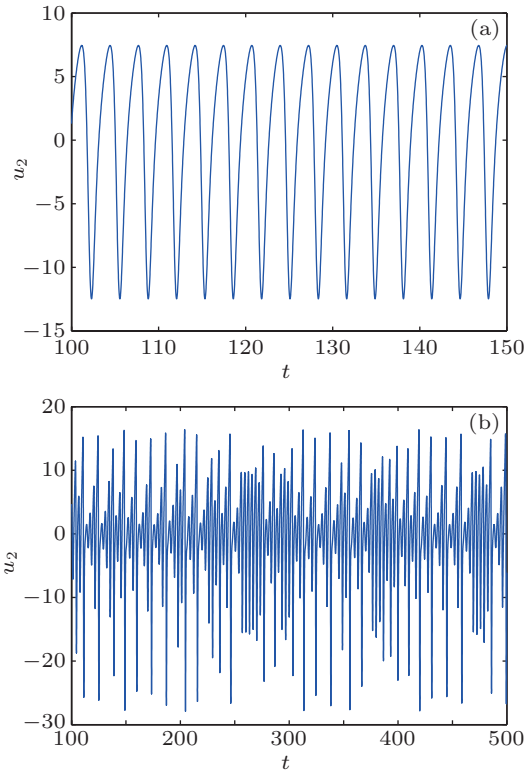


Fig. 12. (color online) (a) Periodic voltage u_2 generated from the oscillator; (b) chaotic voltage u_2.

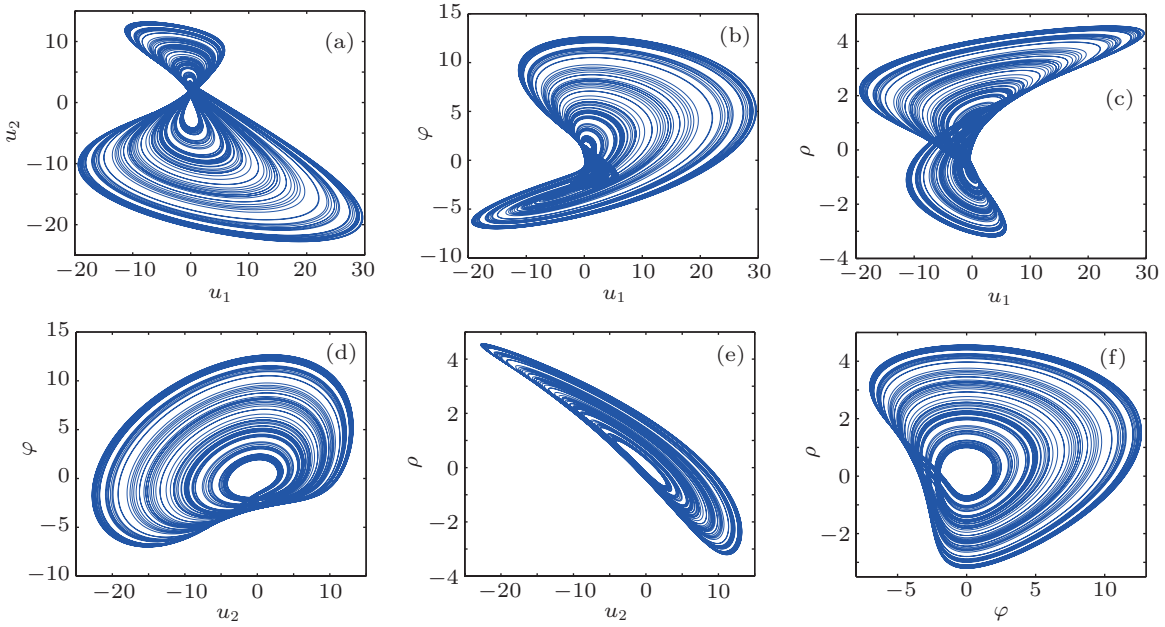


Fig. 13. (color online) Chaotic phase portraits for: (a) u_1–u_2; (b) u_1–φ; (c) u_1–ρ; (d) u_2–φ; (e) u_2–ρ; (f) φ–ρ.

3.2. Co-existent oscillation and co-existent chaotic attractor

The co-existent oscillation is the oscillation that can generate different types of signals with different initial values of the state variables under the same circuit parameters. The so-called different types of signals are periodic, quasi-periodic, chaotic signals as well as equilibrium points. The attractor generated from the co-existent oscillation is called a co-

existent attractor.[23,24]

There are two types of co-existent oscillations. One is the homogeneous oscillations which have the same oscillation types but with different trajectories in their phase space, such as two chaotic oscillations started from two different sets of initial values with the same parameters. Another is the inhomogeneous oscillations which have different oscillation types with different initial values, such as periodic and chaotic oscillations started from two different sets of initial values with the same parameters. Our analysis indicates that the dynamical states of Eq. (12) depend on the setting of the initial conditions, that is, it has multi-stable modes under different initial conditions. So the system can turn from a chaotic state to a periodic state or even a stable equilibrium point when only its initial conditions are changed. When the parameters are set to be $a = 1.0$, $b = 6.0$, $c = 4.5$, $d = 0.77$, $e = 4.0$, and $f = 1.0$, the Lyapunov exponent spectrum with changing $u_1(0)$ in the initial condition $(u_1(0), 0.01, 0.01, 0.01)$ and the corresponding bifurcation diagram are shown in Fig. 14.

From Fig. 14, we can see that as the initial value $u_1(0)$ is varied, the system shows different dynamical behaviors, that is, co-existent attractors appear. In particular, when $u_1(0)$ is varied in the range [0, 1.8], the system is in a chaotic state with a positive Lyapunov exponent; with $u_1(0)$ in the range [1.8, 9.2], the system is in a periodic state with a maximal zero Lyapunov exponent; when $u_1(0)$ is varied in the range [9.2, 10], all the Lyapunov exponents are negative, implying that it is in a stable state. Note that the system undergoes an inverse period-doubling bifurcation in the periodic region of $u_1(0)$.

Figure 15 describes the evolution process of several typical attractors, and Table 1 shows the initial values used. Similarly, when $u_2(0)$, $\varphi(0)$, and $\rho(0)$ are varied, the dynamical behaviors of the system will also change with different oscillations.

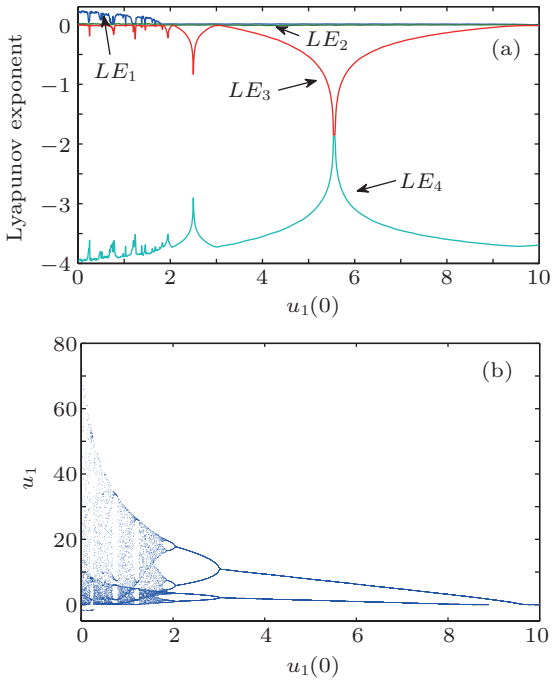


Fig. 14. (color online) (a) Lyapunov exponent spectrum with initial value $u_1(0)$; (b) the corresponding bifurcation diagram.

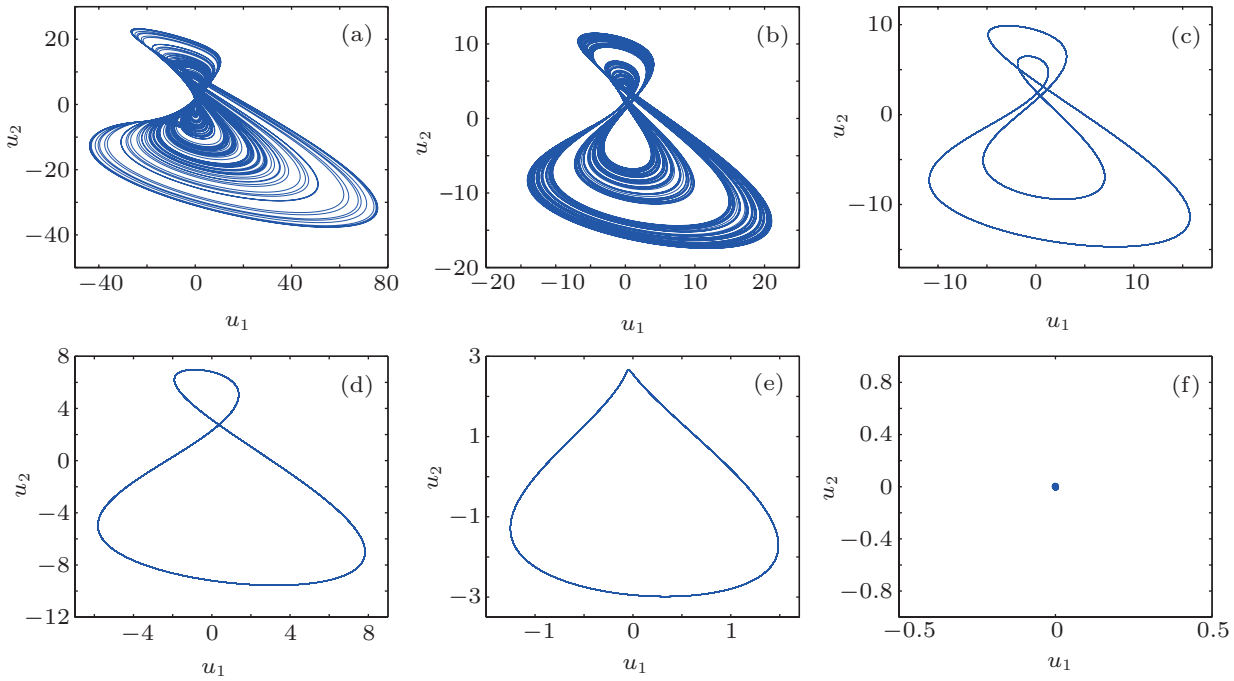


Fig. 15. (color online) Evolution process vs. $u_1(0)$ of co-existent oscillations: (a) chaotic oscillation with $u_1(0) = 0.01$; (b) quasi chaotic oscillation with $u_1(0) = 2.0$; (c) period-2 oscillation with $u_1(0) = 2.5$; (d) period-1 oscillation with $u_1(0) = 5.0$; (e) period-1 oscillation with $u_1(0) = 9.0$; (f) stable equilibrium point with $u_1(0) = 9.9$.

Table 1. Initial values and corresponding states of Fig. 15.

Panel	Initial values	State of attractors
(a)	(0.01, 0.01, 0.01, 0.01)	chaotic state
(b)	(2.0, 0.01, 0.01, 0.01,)	periodic state
(c)	(2.5, 0.01, 0.01, 0.01)	periodic state
(d)	(5.0, 0.01, 0.01, 0.01)	periodic state
(e)	(9.0, 0.01, 0.01, 0.01)	periodic state
(f)	(9.9, 0.01, 0.01, 0.01)	stable state

The attractive basin, which changes with the system parameters, is an important tool to analyze co-existent attractors of circuits. Figure 16 gives the attractive basin of the proposed oscillation circuit in the cross section of $\varphi = 0.01$ and $\rho = 0.01$ when $a = 1.0$, $b = 6.0$, $c = 4.5$, $d = 0.77$, $e = 4.0$, and $f = 1.0$. It includes six different color regions, representing six different types of attractors in the given value regions of the two parameters. From the graph of the attractive basin, we can see that the oscillation state varies with the increases of $u_1(0)$ and $u_2(0)$. Several detailed co-existent attractors are given in Fig. 17. Figure 17(a) belongs to the type of co-existence of two different chaotic attractors. Figure 17(b) belongs to the type of chaotic attractor and limit cycle. Figure 17(c) belongs to the type of co-existence of two different limit cycles. Figure 17(d) belongs to the type of limit cycle and stable equilibrium points. Thus, figures 17(a) and 17(c) show homogeneous co-existent attractors, while figures 17(b) and 17(d) show inhomogeneous co-existent attractors. Table 2 lists the initial values and the corresponding types of co-existent attractors.

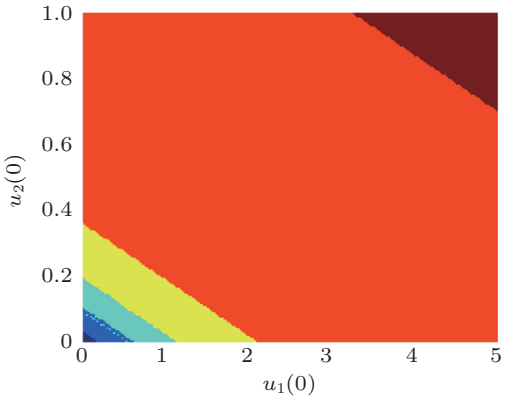


Fig. 16. (color online) Attractive basin on the cross section of $\varphi = 0.01$ and $\rho = 0.01$, with $a = 1.0$, $b = 6.0$, $c = 4.5$, $d = 0.77$, $e = 4.0$, and $f = 1.0$.

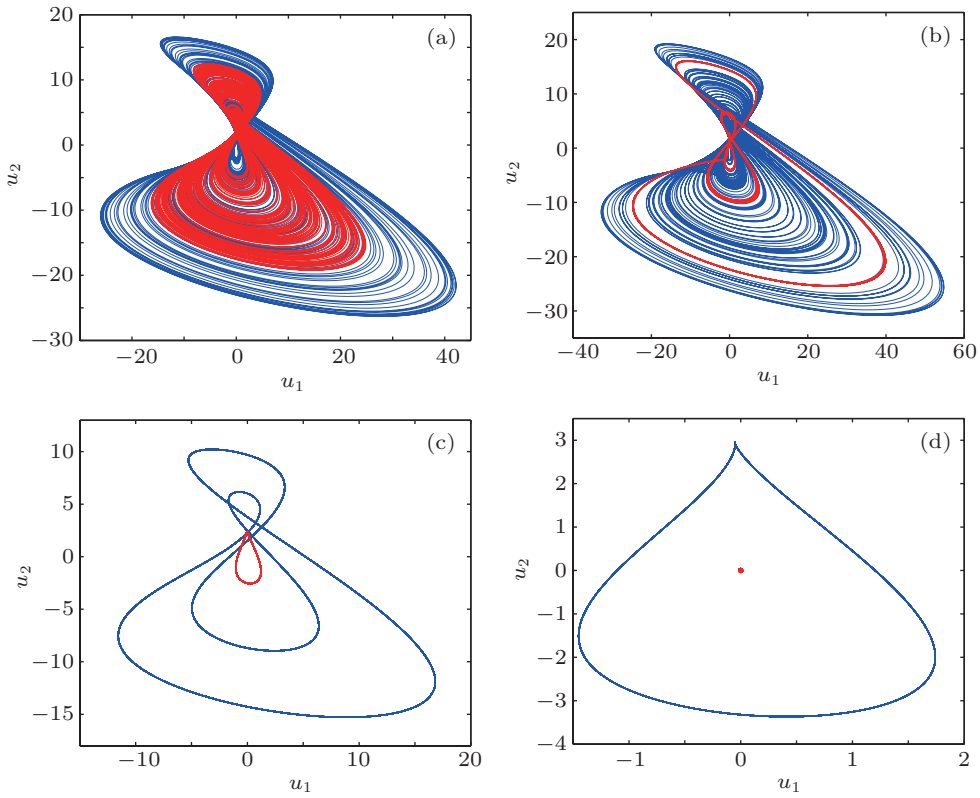


Fig. 17. (color online) (a) and (c) Homogeneous co-existent attractors; (b) and (d) inhomogeneous co-existent attractors.

Table 2. Initial values and corresponding types of co-existent attractors of Fig. 17.

Panel	Initial values	State of attractors
(a)	(0.4510 0.0100 0.01 0.01), (0.9000 0.0800 0.01 0.01)	co-existence of two chaotic attractors
(b)	(0.2261 0.0050 0.01 0.01), (0.5779 0.0000 0.01 0.01)	co-existence of chaotic attractors & limit cycle
(c)	(2.3367 0.0000 0.01 0.01), (5.0000 0.7186 0.01 0.01)	co-existence of two limiting cycles
(d)	(4.3000 0.7900 0.01 0.01), (4.9000 0.8600 0.01 0.01)	co-existence of limit circle & stable points

4. Dimension reduction analysis

4.1. Dimension reduction equations of the oscillator

For the purpose of reducing the complexity of solving Eq. (12), by integrating with respect to t at both sides of Eq. (11), and assuming all the initial values of the integrals are zero, we can change Eq. (11) to the following solvable 3-dimensional equations:

$$\begin{cases} \dfrac{\mathrm{d}\varphi_1}{\mathrm{d}t} = \dfrac{1}{C_1}\left(q_{\mathrm{M}} - \dfrac{\varphi_1}{R}\right), \\ \dfrac{\mathrm{d}\varphi_2}{\mathrm{d}t} = \dfrac{1}{C_2}(G\varphi_2 - q_{\mathrm{M}}), \\ \dfrac{\mathrm{d}\rho_{\mathrm{M}}}{\mathrm{d}t} = \varphi_2 - \varphi_1, \end{cases} \tag{13}$$

where $\varphi_1 = \int_{t_0}^{t} u_1(\tau)\mathrm{d}\tau$ is the flux of C_1, $\varphi_2 = \int_{t_0}^{t} u_2(\tau)\mathrm{d}\tau$ is the flux of C_2, and $\rho_{\mathrm{M}} = \int_{t_0}^{t} \varphi_{\mathrm{M}}(\tau)\mathrm{d}\tau$ is the integral of the flux through the meminductor L_{M}. By inserting $q_{\mathrm{M}} = \alpha\rho_{\mathrm{M}} + \beta\rho_{\mathrm{M}}^2/2$ into Eq. (13) and setting $x = \varphi_1$, $y = \varphi_2$, $z = \rho_{\mathrm{M}}$, $a = \alpha/C_1$, $b = \beta/(2C_1)$, $c = 1/(C_1R)$, $d = G/C_2$, $e = \alpha/C_2$, $f = \beta/(2C_2)$, equation (13) can be rewritten as

$$\begin{cases} \dot{x} = az + bz^2 - cx, \\ \dot{y} = dy - ez - fz^2, \\ \dot{z} = y - x. \end{cases} \tag{14}$$

When $a = 1.0$, $b = 20.0$, $c = 4.0$, $d = 0.8$, $e = 4.0$, and $f = 2.0$, system (14) is a chaotic oscillator with the phase portraits shown in Fig. 18, where panel (d) is the relationship of ρ and q. Its Lyapunov exponents are computed as

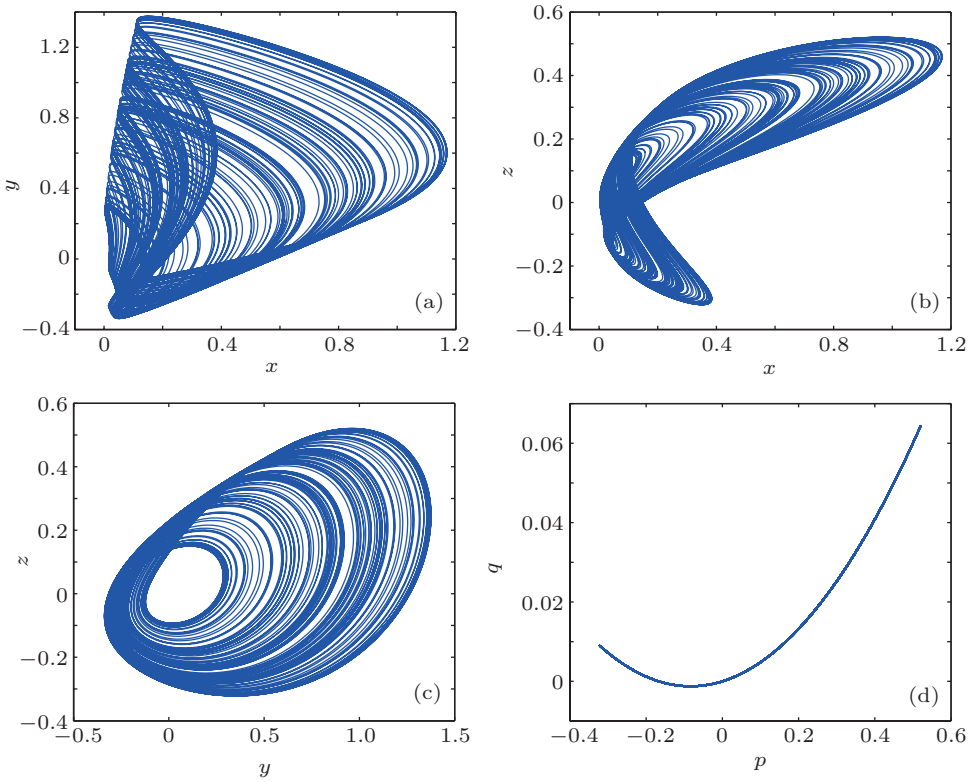


Fig. 18. (color online) (a) Chaotic phase portraits on (a) x–y, (b) x–z, and (c) y–z planes; (d) relationship of ρ and q.

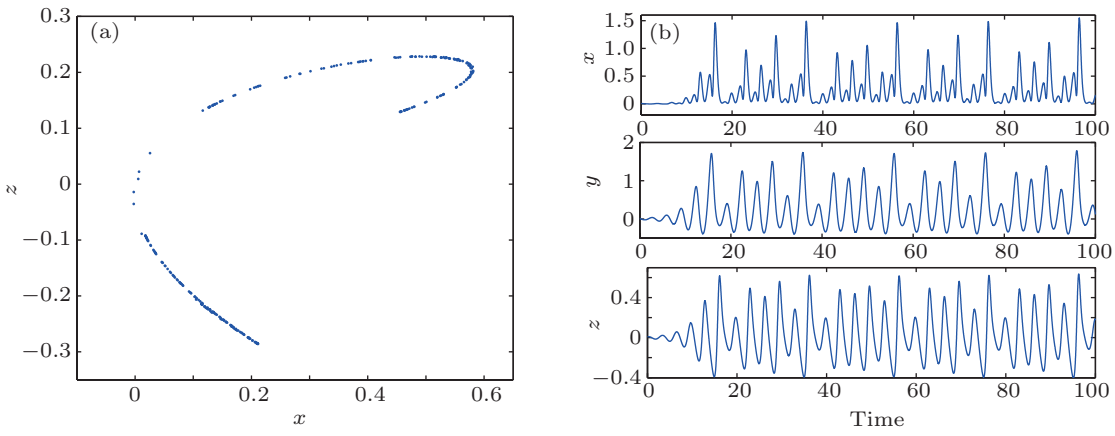


Fig. 19. (color online) (a) Poincaré map projected onto the x–z plane; (b) chaotic oscllation waveforms of the meminductor-based oscillator.

$LE_1 = 0.1106$, $LE_2 = 0$, and $LE_3 = -3.3106$. The projection of the 3-dimensional Poincaré map onto the x–z plane is shown in Fig. 19(a), and the time domain waveforms of the three state variables are shown in Fig. 19(b).

4.2. Dissipativeness and stability of the oscillator

The divergence of system (14) can be expressed as

$$\nabla V = \frac{\partial \dot{x}}{\partial x} + \frac{\partial \dot{y}}{\partial y} + \frac{\partial \dot{z}}{\partial z} = -c + d.$$

If $\nabla V = -c + d < 0$, the system is dissipative. Therefore, besides periodic oscillation, to make sure there will be chaotic oscillations included, the condition should be $c > d$.

Let $\dot{x} = \dot{y} = \dot{z} = 0$, we can obtain equilibrium points $E_1(0,0,0)$ and $E_2\left(\frac{az_0+bz_0^2}{c}, \frac{az_0+bz_0^2}{c}, z_0\right)$, where $z_0 = (ad - ce)/(cf - bd)$. When system (14) is linearized at equilibrium point $E_1(0,0,0)$, we have the Jacobian matrix

$$\boldsymbol{J} = \begin{bmatrix} -c & 0 & a \\ 0 & d & -e \\ -1 & 1 & 0 \end{bmatrix}. \tag{15}$$

The according characteristic equation is

$$\lambda^3 + (c-d)\lambda^2 + (a+e-cd)\lambda + ce - ad = 0.$$

By the Routh–Hurwitz rule, we conclude that if

$$\Delta_1 = c - d,\ \ \Delta_2 = (ac - ed + cd^2 - c^2 d)/(c-d),\ \ \Delta_3 = ce - ad$$

are all positive, the eigenvalues of the system are all negative, and the system is stable. When the parameters are $a = 1.0$, $b = 20.0$, $c = 4.0$, $d = 0.8$, $e = 4.0$, and $f = 2.0$, we have $\lambda_1 = -3.7853$ and $\lambda_{23} = 0.2926 \pm 1.9824\mathrm{i}$. λ_1 is a negative real number, and λ_2 and λ_3 are a pair of conjugate complex numbers with a positive real part, so E_1 is an unstable saddle point.

When system (14) is linearized at equilibrium point E_2, we have the Jacobian matrix

$$\boldsymbol{J} = \begin{bmatrix} -c & 0 & a + 2bz_0 \\ 0 & d & -e - 2fz_0 \\ -1 & 1 & 0 \end{bmatrix}. \tag{16}$$

The corresponding characteristic equation is

$$\lambda^3 + a_1\lambda^2 + a_2\lambda + a_3 = 0,$$

where $a_1 = c - d$, $a_2 = a + e + 2bz_0 + 2fz_0 - cd$, and $a_3 = ce - ad + 2cfz_0 - 2bdz_0$. When $\Delta_1 = a_1$, $\Delta_2 = (a_1a_2 - a_3)/a_1$, and $\Delta_3 = a_3$ are not all positive, it is possible to produce a chaotic oscillation. Let $a = 1.0$, $b = 20.0$, $c = 4.0$, $d = 0.8$, $e = 4.0$, and $f = 2.0$, the corresponding eigenvalues are $\lambda_1 = 0.1768$ and $\lambda_{23} = -1.6884 \pm 9.1185\mathrm{i}$. λ_1 is a positive real root, λ_2 and λ_3 are a pair of conjugate complex roots with a negative real part, so it is also an unstable equilibrium point.

4.3. Dynamical properties with varying a

Let $a = \alpha/C_1$ in Eq. (14), where $\alpha = 0.03$ is kept constant, then the value of a depends on the parameter C_1. With varying a , the system will be in different states because of the change of the equilibrium point stability. When a is varied in the region [1, 2], the corresponding Lyapunov exponent spectrum is shown in Fig. 20(a) (all the values of LE_3 are less than -3, for the purpose of clarity, the third curve of the Lyapunov exponent is not shown). The bifurcation diagram of x varying with a is illustrated in Fig. 20(b).

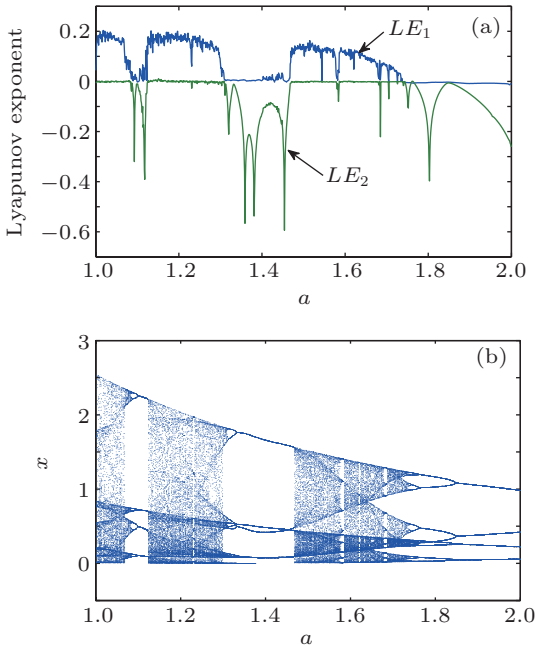


Fig. 20. (color online) (a) Lyapunov exponent spectrum with respect to a; (b) bifurcation diagram with respect to a.

From Fig. 20, we can see that the oscillator undergoes the process from the abruptly chaotic oscillation to periodic oscillation by an anti period-doubling bifurcation, then to chaotic oscillation again, and at last it goes to a stable periodic state via the repeated bifurcations from chaos to period. Note that when $a = 1$, a chaotic oscillation called abrupt chaos suddenly emerges.

4.4. Dynamical properties with varying d

In Eq. (14), by only varying d, the system will be in different states. When d is varied in the interval [0.1, 1], the resulted Lyapunov exponent spectrum and the corresponding bifurcation diagram of x are shown in Fig. 21.

From Fig. 21, we can see that the system can generate multiple periodic oscillations and chaotic oscillations through a complex bifurcation process. When $d \in [0.1, 0.22]$, it is in the period-1 state; when $d \in [0.22, 0.78]$, it is in the period-doubling bifurcation process, and when $d \in [0.78, 1]$, it is in the chaotic state but with several periodic windows. The typical phase portraits with varying d are depicted in Fig. 22, where the complex bifurcation that changes from equilibrium point to period-1 and to period-2, then to period-4, and at last to chaos are observed clearly.

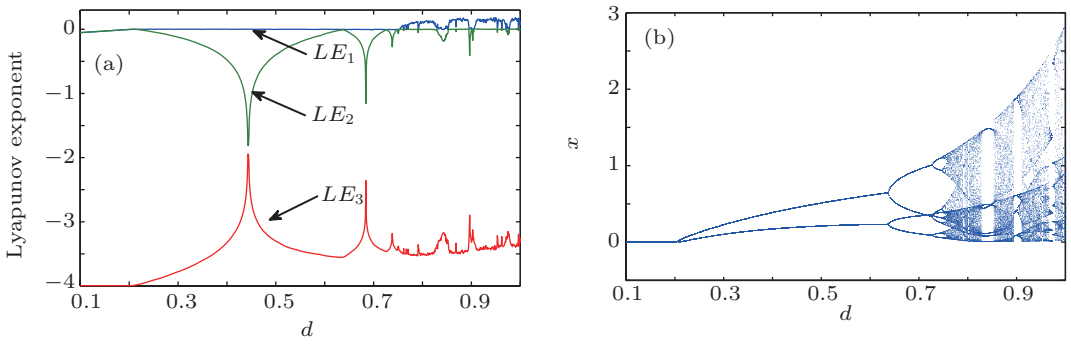


Fig. 21. (color online) (a) Lyapunov exponent spectrum with respect to d; (b) bifurcation diagram with respect to d.

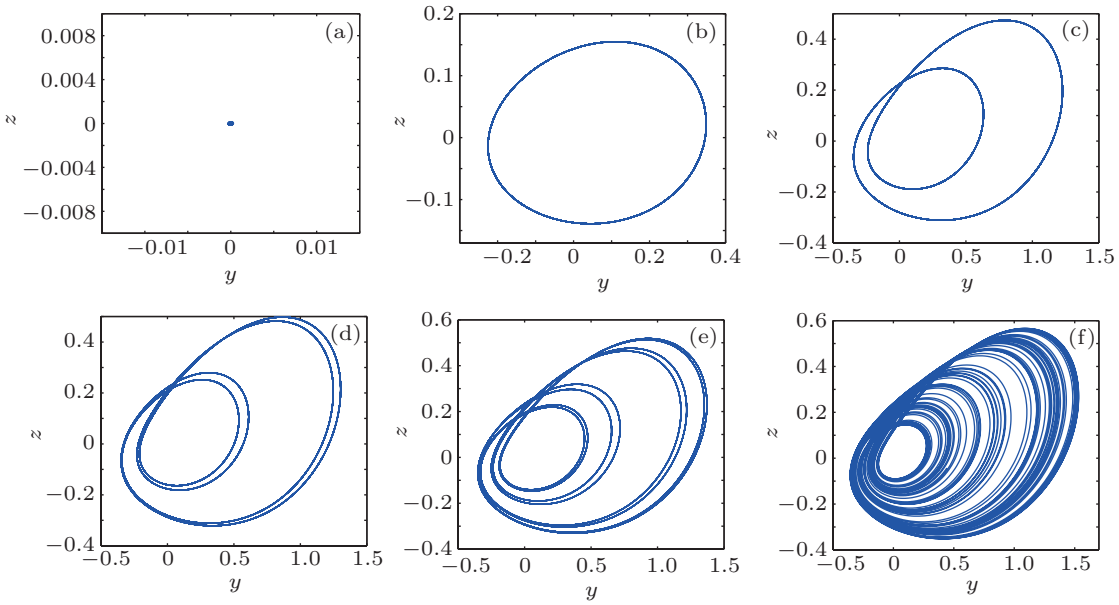


Fig. 22. (color online) (a) Equilibrium point with $d = 0.17$; (b) period-1 with $d = 0.25$; (c) period-1 with $d = 0.7$; (d) period-2 with $d = 0.73$; (e) period-4 with $d = 0.75$; (f) chaos with $d = 0.8$.

4.5. Dynamical map with varying c and d

The bifurcation parameters c and d impact the dynamical properties of the system. The dynamical map can present the impact on the dynamical properties of the system, from which we can obtain the dynamical state with detailed parameter ranges. Figure 23 gives the two-dimensional dynamical map with respect to c and d, in the meantime, it describes the dependent relationship between the dynamical behaviors and the bifurcation parameters. In the dynamical map, we set $a = 1.0$, $b = 20.0$, $e = 4.0$, and $f = 2.0$.

In Fig. 23, the blue area marked C represents that the system is in the chaotic state; the yellow area marked P represents that the system is in the periodic state; while the red area marked S stands for the stable state. This dynamical map depicts the impact of the parameters on the dynamical behavior of the system visually. When $d \in [0.1, 0.2]$, the system converges to point attractors; when $d \in [0.2, 0.8]$, the system runs at periodic orbits; while when $d \in [0.8, 1]$, the system is in chaotic states.

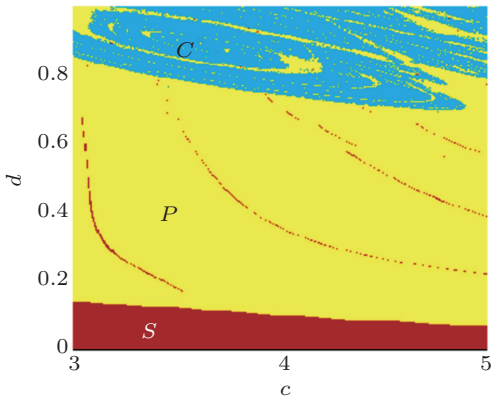


Fig. 23. (color online) Dynamical map with respect to bifurcation parameters c and d.

By inserting $a = 1.0$, $b = 20.0$, $e = 4.0$, and $f = 2.0$ into Eq. (14), and linearizing it around equilibrium point $E_1(0,0,0)$, we obtain the characteristic equation

$$\lambda^3 + (c-d)\lambda^2 + (5-cd)\lambda + 4c - d = 0.$$

By the Routh–Hurwitz rule, we conclude that when

$cd(c-d)+4d-c<0$, equilibrium point E_1 is stable and this system will converge into point attractors (as shown in Fig. 22(a)). The bifurcation border line between the red region and the yellow region at the bottom of Fig. 23 is determined by

$$cd(c-d)+4d-c=0.$$

The stable equilibrium points stand in the area below the line, because the stable area must satisfy $cd(c-d)+4d-c<0$.

4.6. Dynamical map with varying a and e

Figure 24 gives the dynamical map defined by a and e, where we set the other parameters to be $b=20.0$, $c=4.36$, $d=0.97$, and $f=2.0$. There are two different areas with different colors in Fig. 24, where the blue area marked C and the yellow area marked P represent chaotic and periodic states, respectively. Thus when a is small, the system is in the chaotic state; as a gets large, it transfers from chaotic orbit to period orbit.

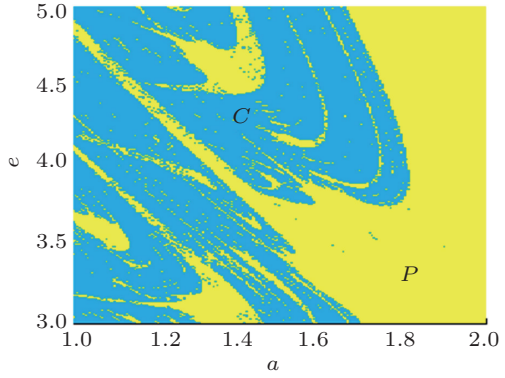


Fig. 24. (color online) Dynamical map defined by bifurcation parameters a and e.

5. Realization of the meminductor-based oscillator

By combining Eq. (14) and the equivalent circuit model of the meminductor in Fig. 3, we design an equivalent circuit of the meminductor-based oscillator and verify the circuit by experiments. The designed circuit is shown in Fig. 25 and the according simulation results by using Multisim are shown in Fig. 26.

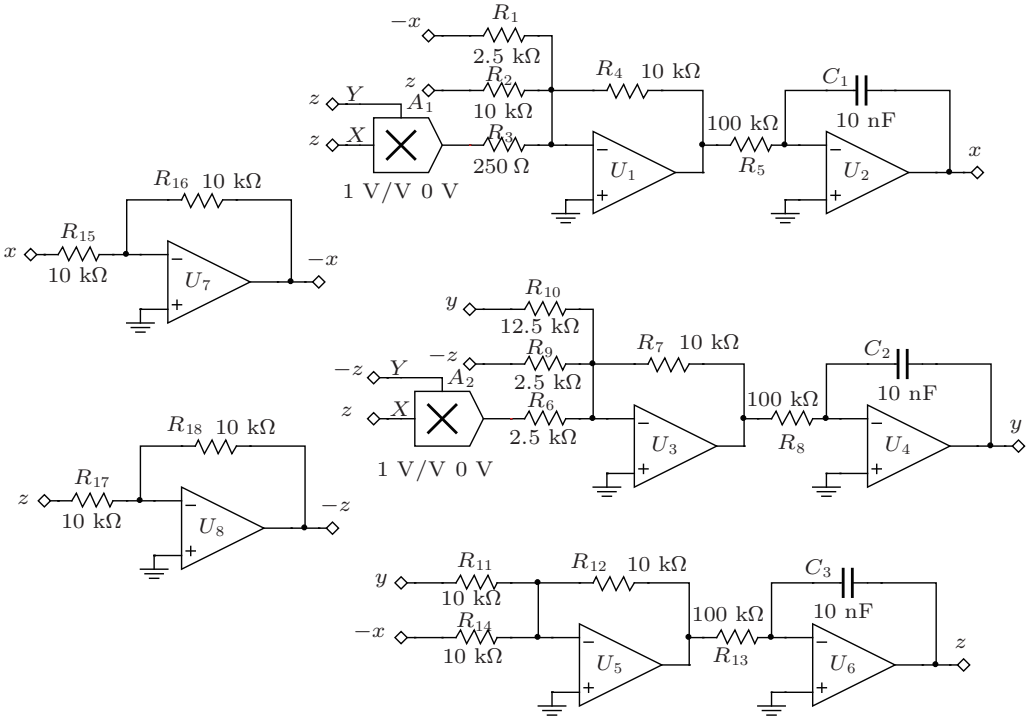


Fig. 25. Equivalent circuit of the meminductor-based chaotic oscillator.

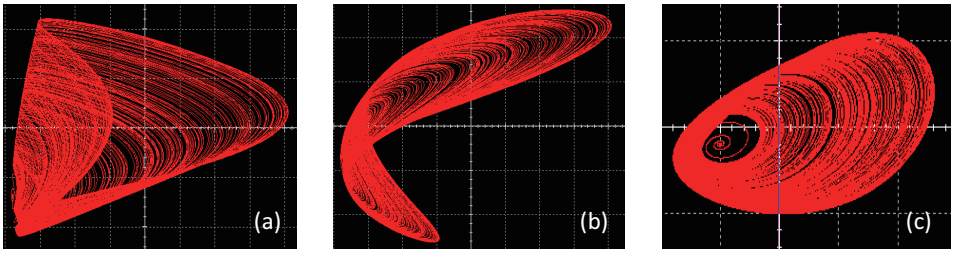


Fig. 26. (color online) (a) Phase obits of (a) x–y, (b) x–z, (c) y–z for the meminductor-based oscillator.

The equivalent circuit is designed based on the state equation (14). In Fig. 25, U_1–U_8 are operational amplifiers used for implementing the operations of inverse proportion, integration, and add for variables x, y, and z; and A_1 and A_2 are multipliers used for implementing z^2. According to Fig. 25, the state equations can be described as

$$\begin{cases} \dfrac{\mathrm{d}X}{\mathrm{d}T} = \dfrac{1}{R_5C_1}\left(\dfrac{R_4}{R_2}Z + \dfrac{R_4}{R_3}Z^2 - \dfrac{R_4}{R_1}X\right), \\ \dfrac{\mathrm{d}Y}{\mathrm{d}T} = \dfrac{1}{R_8C_2}\left(\dfrac{R_7}{R_{10}}Y - \dfrac{R_7}{R_9}Z - \dfrac{R_7}{R_6}Z^2\right), \\ \dfrac{\mathrm{d}Z}{\mathrm{d}T} = \dfrac{1}{R_{13}C_3}\left(\dfrac{R_{12}}{R_{11}}Y - \dfrac{R_{12}}{R_{14}}X\right). \end{cases} \tag{17}$$

We apply time and scale transformations for Eq. (17), and let $t = KT$, $x = MX$, $y = MY$, $z = MZ$, where $K = 1000$ and $M = 2$ are the scale transformation factors. Then equation (1) is transformed to

$$\begin{cases} \dfrac{\mathrm{d}x}{\mathrm{d}t} = \dfrac{1}{KR_5C_1}\left(\dfrac{R_4}{R_2}z + \dfrac{R_4}{MR_3}z^2 - \dfrac{R_4}{R_1}x\right), \\ \dfrac{\mathrm{d}y}{\mathrm{d}t} = \dfrac{1}{KR_8C_2}\left(\dfrac{R_7}{R_{10}}y - \dfrac{R_7}{R_9}z - \dfrac{R_7}{MR_6}z^2\right), \\ \dfrac{\mathrm{d}z}{\mathrm{d}t} = \dfrac{1}{KR_{13}C_3}\left(\dfrac{R_{12}}{R_{11}}y - \dfrac{R_{12}}{R_{14}}x\right). \end{cases} \tag{18}$$

Comparing Eqs. (18) and (14), we have

$$\begin{aligned} &a = R_4/KR_5C_1R_2, \quad b = R_4/KMR_5C_1R_3, \\ &c = R_4/KR_5C_1R_1, \quad d = R_7/KR_8C_2R_{10}, \\ &e = R_7/KR_8C_2R_9, \quad f = R_7/KMR_8C_2R_6, \\ &R_{12}/KR_{13}C_3R_{11} = R_{12}/KR_{13}C_3R_{14} = 1. \end{aligned}$$

When $C_1 = C_2 = 10$ nF, $R_1 = R_6 = R_9 = 2.5$ kΩ, $R_2 = R_4 = R_7 = R_{11} = R_{12} = R_{14} = R_{15} = R_{16} = R_{17} = R_{18} = 10$ kΩ, $R_3 = 250$ Ω, $R_5 = R_8 = R_{13} = 100$ kΩ, and $R_{10} = 12.5$ kΩ, the corresponding parameters are $a = 1.0$, $b = 20.0$, $c = 4.0$, $d = 0.8$, $e = 4.0$, and $f = 2.0$. The simulated phase orbits for the circuit are shown in Fig. 26.

The experimental meminductor-based oscillator obtained according to Fig. 25 is depicted in Fig. 27, where R_1 and R_{10} are variable resistors. We can change the resistances of R_1 and R_{10} to change the state of the output of the oscillator. When $R_1 = 2.86$ kΩ and the other parameters are the same as above, the oscillator can produce a double-period signal, the corresponding oscilloscope displays are shown in Figs. 28(a), 28(c), and 28(e) (oscilloscope DSO1302A was used). When $R_1 = 2.5$ kΩ, the oscillator will produce chaotic obits, which are shown in Figs. 28(b), 28(d), and 28(f). The dynamical properties of the circuit can be changed by adjusting the value of R_1. Figure 29 demonstrates a series of phase portraits of y–z in different states. Figure 30 demonstrates the experimental setup.

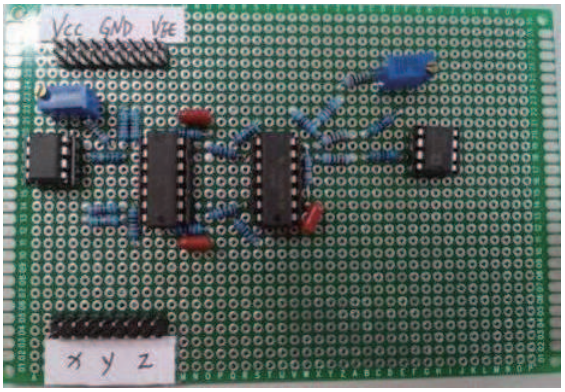


Fig. 27. (color online) Experimental circuit board of the meminductor-based oscillator.

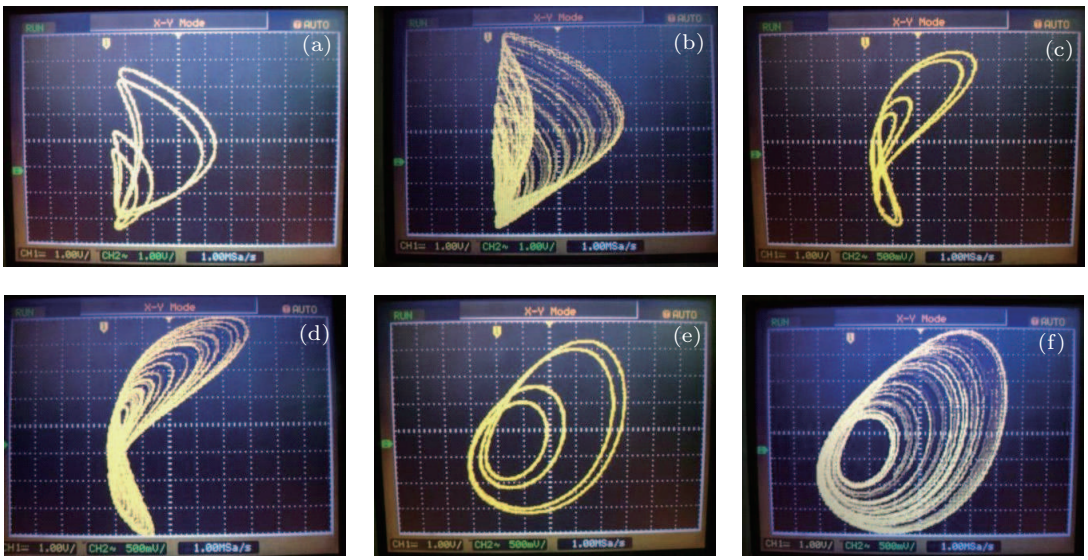


Fig. 28. (color online) (a) Experimental periodic orbit of x–y; (b) experimental chaotic orbit x–y; (c) experimental periodic orbit of x–z; (d) experimental chaotic orbit of x–z; (e) experimental periodic orbit of y–z; (f) experimental chaotic orbit of y–z.

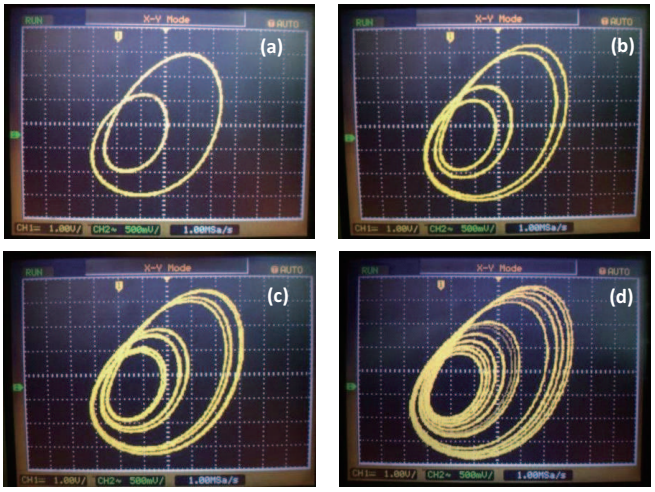


Fig. 29. (color online) Experimentally observed bifurcations: (a) experimental period-1 orbit with $R_1 = 3.3$ kΩ; (b) experimental period-2 orbit with $R_1 = 2.85$ kΩ; (c) experimental period-4 orbit with $R_1 = 2.81$ kΩ; (d) experimental chaotic orbit with $R_1 = 2.78$ kΩ.

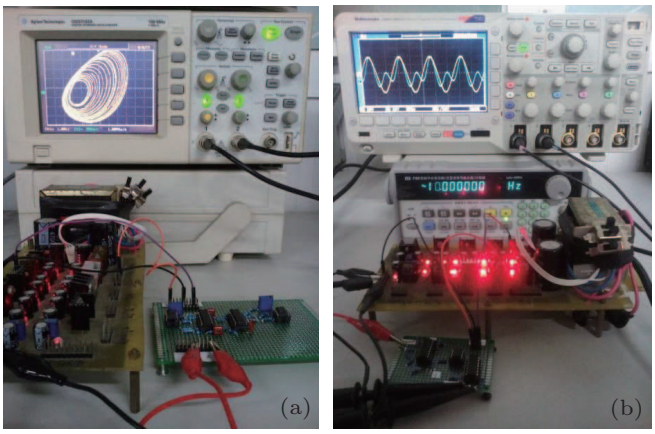


Fig. 30. (color online) (a) Experimental setup of meminductor-based oscillator; (b) experimental setup of the meminductor model.

6. Conclusion

A mathematical model of the flux-controlled meminductor and its equivalent circuit models of φ–i and ρ–q have been presented. In the circumstance that a physical meminductor has not been realized, we can use such models instead of the real meminductor for studying the properties and applications of meminductors theoretically and experimentally. On the other hand, based on the model, we have designed and built a memintuctor-based oscillator, which exhibits some complex behaviors, such as co-existent oscillations, abrupt chaos, period-doubling bifurcation, inverse period-doubling bifurcation, and broader chaotic attractive field. Especially, it is sensitive to the initial conditions which could be used to produce co-existent oscillations and to generate consecutive and stable pseudo random sequences as multi sources, which can be applied in information encryption and secret communications.

References

[1] Chua L O 1971 *IEEE Trans. Circuit Theory* **18** 507
[2] Strukov D B, Snider G S, Stewart D R and Williams R S 2008 *Nature* **453** 80
[3] Chua L O 1978 *Guest Lectures of the 1978 European Conference on Circuit Theory and Design* 81
[4] Chua L O 2003 *Proc. IEEE* **91** 1830
[5] Di Ventra M, Pershin Y V and Chua L O 2009 *Proc. IEEE* **97** 1717
[6] Chua L O 2009 *IEEE Expert Now SHORT Course* [Online] Available at:
http: //ieeexplore.ieee.org/xpl/modulesabstract.jsp?mdnumber=EW1091
[7] Jung C M, Choi J M and Min K S 2012 *IEEE Trans. Nanotechnol.* **11** 611
[8] Eshraghian K, Cho K R, Kavehei O, Kang S K, Abbott D and Steve S M 2011 *IEEE Trans. Vlsi Systa.* **19** 1407
[9] Bao B C, Liu Z and Xu J P 2010 *Chin. Phys. B* **19** 030510
[10] Bao B C, Hu F W, Liu Z and Xu J P 2014 *Chin. Phys. B* **23** 070503
[11] Xu B R 2013 *Acta Phys. Sin.* **62** 190506 (in Chinese)
[12] Fouda M E and Radwan A G 2014 *Microelectron J.* **45** 1372
[13] Pershin Y V and Di Ventra M 2011 *Adv. Phys.* **60** 145
[14] Biolek D, Biolek Z and Biolkova V 2011 *Circ. Sig. Process.* **66** 129
[15] Liang Y, Yu D S and Chen H 2013 *Acta Phys. Sin.* **62** 158501 (in Chinese)
[16] Abdelouahab M S, Lozi R and Chua L O 2014 *Int. J. Bifurcation Chaos* **24** 1430023
[17] Pershin Y V and Di Ventra M 2010 *Electron. Lett.* **46** 517
[18] Shi Z Y, Wang C L, Bao B C and Feng F 2014 *UEST C* **43** 845
[19] Sah M P, Budhathoki R K, Yang C and Kim H 2014 *Circuit ISCAS* **33** 2363
[20] Pershin Y V and Di Ventra M 2011 *Adv. Phys.* **60** 145
[21] Kim K M, Jeong D S and Hwang C S 2011 *Nanotechnology* **22** 254002
[22] Muthuswamy B and Chua L 2010 *Int. J. Bifurcation Chaos* **20** 1567
[23] Sprott J C, Wang X and Chen G 2013 *Int. J. Bifurcation Chaos* **23** 1350093
[24] Molaie M, Jafari S, Sprott J C and Hashemi S M R H 2013 *Int. J. Bifurcation Chaos* **23** 1350188